Experiments in Fluids (2023) 64:32
https://doi.org/10.1007/s00348-023-03576-0

RESEARCH ARTICLE

New method to separate turbulence statistics of fan rotor wakes from background flow

Luciano Caldas[1] · Robert Meyer[1]

Received: 30 June 2022 / Revised: 2 December 2022 / Accepted: 8 January 2023 / Published online: 24 January 2023

Abstract

The separation of turbulence parameters such as turbulence intensity and integral length scale of fan rotor wakes from background flow from unsteady velocity data is a challenge. The two processes are overlapped, and typically, very few samples of the data are taken inside the rotor wakes, making it hard to perform any spectral analysis. This work proposes a new time domain approach to separate the two processes by using two suitable data tapers. The unsteady velocity cyclic variance distribution is used as reference to establish the border between the blade wakes and the background flow. Results indicate an increase in wake turbulence levels and a slight increase in background turbulence levels with the increase in fan blade loading. The integral length scale of the rotor wakes did not change considerably among the different fan loading analyzed. This contrasts with the values observed for the background flow, which decreased with increasing of fan loading. The rotor wakes seem to be anisotropic, regardless of the fan operating point.

Graphical abstract

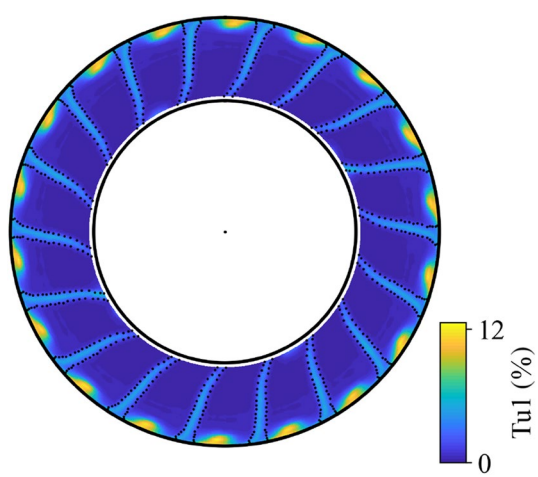

1 Introduction

In the sake of making aircraft environmentally greener, it is envisaged not only more efficient aircraft with lower greenhouse gas emissions, but they should also be quieter. Aircraft noise has received increased attention in the past decades due to the high demand for flights combined with the growth of towns nearby airports (Envia 2018). The pressure to not only reduce aircraft noise emissions, but also make them more efficient makes the need to focus on one critical source

✉ Luciano Caldas
Luciano.Caldas@dlr.de

Robert Meyer
Robert.Meyer@dlr.de

[1] Engine Acoustics, German Aerospace Center - DLR, Mueller-Breslau-Str. 8, 10623 Berlin, Germany

of aircraft noise during approach and take-off: the engines (Astley et al. 2007; Airbus 2003). In modern Ultra-High Bypass Ratio (UHBR) turbofan engines, the rotor (fan)–stator interaction noise is the main contributor to the total engine noise emissions.

Fan noise emission is strongly dependent on the turbulence characteristics of the flow. Broadband noise generation arises due to the interaction of the flow turbulence with the leading edges of both the rotor blades and the stator vanes (Kholodov et al. 2021; Lewis et al. 2020). The increase in inflow turbulence levels leads to an increase in both the rotor self-noise and the rotor–stator interaction broadband noise (Preisser and Chestnutt 1984). The rotor–stator interaction noise is mainly dependent on the rotor wake turbulence properties, such as wake width, velocity deficit, turbulence intensity levels, and turbulence integral length scale (ILS). However, the assessment of these properties is by no means trivial. Both the measurement of the turbulence field downstream a rotating fan and the data processing associated with these data to extract turbulence information are not straight forward. Alongside with that, only a few references are found in the literature regarding the assessment and extraction of turbulence properties of rotor wakes.

The turbulence parameters of the flow are typically summarized in terms of turbulence intensity (or equivalently turbulent kinetic energy) and the turbulence integral length scale. The first is a measure relating the root mean square (RMS) of the velocity fluctuations from a given unsteady velocity signal. The second is associated with the size of the most energetic eddies in a turbulent field, or the size of the most energetic "vortices."

In order to understand fan noise emission mechanisms, as well as to predict fan noise levels, the complete characterization of the flow regarding these turbulence parameters shall be performed. The flow has to be characterized both in the inlet of the engine, upstream the fan, and also downstream the fan, the region called interstage (between fan and stator). The most common way to access the turbulence field is by means of hot-wire anemometry (Lengyel-Kampmann et al. 2012; Meillard et al. 2013; Meyer et al. 2015, 2019). This technique allows the measurement of the turbulent flow field at a specific position in space. The turbulence captured by the sensors refers to the turbulence properties of a tiny volume delimited roughly by the length of the wires used, which are typically around 2 mm long.

For hot-wire measurements performed in the interstage section, the hot-wire sensors are mounted a fraction of the blade chord length downstream of the rotor and traversed in the radial direction. The signals acquired are therefore composed of the periodic blade wakes generated by the rotating fan and the background flow between them. The problem therefore is: how to separate the turbulent information arising from the rotor wakes and from the background flow. In order to shed some light in this gap, a new technique that allows such separation is proposed and described in details in this article, which is structured as follows: Sect. 2 provides a literature review on turbulence parameters estimation in the interstage section between rotating fan and stator vanes. Section 3 gives an overview of the fan test rig as well as the hot-wire anemometry technique. Section 4 describes the new proposed technique for the separation of the two turbulence processes (rotor wakes and background flow) in the time domain. Section 5 shows the experimental results obtained with the proposed new technique applied to measured data. Section 6 ends the paper with conclusions and remarks.

2 Literature survey on turbulence scale estimation

Evans (1975) analyzed hot-wire data from a compressor rig measured downstream the moving blades. A relevant observation from this work was that the free-stream turbulence levels are lowest near the compressor design point, and increase with decreasing flow coefficient as the compressor operation point moves toward stall condition. This study was one of the pioneers on removing the periodic component of the mean velocity distribution due to the rotor wakes for the correct estimation of the turbulence intensity. It was also observed that turbulent components from the velocity signal become more important than the periodic fluctuations of the mean velocity, when the compressor operating point changes toward stall.

Camp and Shin (1995) performed a series of measurements in three different multistage compressors. Hot-wire measurements were performed downstream of one of the rotors of a multi-stage compressor. For more details about the measurement procedure, please consult the reference. For one compressor configuration, the hot-wire probe was traversed both in radial and circumferential directions, covering two vane passages. In order to suppress the harmonic components arising from the periodic rotor wakes, they proposed estimating the turbulence intensity by transforming the data into the frequency domain by a discrete Fourier transform, setting the BPF tones to zero, and transforming it back to time domain. The integral length scale was obtained by the multiplying the Fourier transformed series by its complex conjugate, transforming it back to time domain, obtaining the auto-correlation function. This function was then integrated giving the equivalent ILS of the signal. This approach allows removing the power due to the periodicity of the rotor wakes from the turbulence power spectrum, but this gives only the averaged parameters (turbulence intensity and ILS) of the respective measurement data.

Lewalle and Ashpis (2004) used the wavelet technique to assess spatial and frequency resolution from the turbulence data measured downstream of a rotating fan. The unsteady velocity signals from hot-wire measurements were segmented in data blocks with size equivalent to a blade passage. The blade passage is defined as the geometric angle between two neighboring blades. The data blocks were averaged in the time domain delivering the average velocity profile of a rotor blade wake. The wavelet transform was then applied into this smoothed signal. Each element from the wavelet spectrum was multiplied by its respective frequency in order to obtain the energy spectrum $f.E(f)$, where f stands for the frequency and $E(f)$ for the wavelet spectrum. The maximum of this energy spectrum is associated with the dominant turbulence scale in the flow. The authors highlighted that this is not the same as the turbulence integral length scale. Formulations for each procedure are different from each other. However, they both are correlated. They found that under Taylor's hypothesis (Pope 2000; Hinze and Clark 1975) and HIT (homogeneous and isotropic turbulence) assumption, for Re > 300 the ratio of the integral scale and dominant scale lies at approx. 0.75.

The wavelet technique is performed into the time-averaged velocity signal, which is equivalent to the coherent component resulted from a cyclostationary analysis, as described in Sect. 4.1. In this case, the turbulence information of the signal is lost by the averaging procedure. What remains is the average shape of the rotor blade wake. The wavelet spectrum will have a shape dependent on the slope of the averaged wake velocity profile, not on the turbulence properties themselves. In our opinion, a potentially better approach could be done by performing the wavelet technique either on the incoherent part of the signal resulted from a cyclostationary analysis, or directly in the resampled signal. After that, the wavelet spectrum of each data block can be averaged for every blade passage. This approach is similar to a Welch power spectrum density estimator (Kay 1993; Percival and Walden 1993), but instead of using a discrete Fourier transform, the Wavelet transform shall be used. In this way, the frequency properties of the signal are averaged out over every blade passage, and not the time domain properties.

Jurdic et al. (2009) used techniques based on the cyclostationarity property of the turbulence signals combined with the Wigner–Ville (Giannakis et al. 1998; Antoni 2007) spectrum to detect cyclic–periodic properties of the turbulence spectrum. The authors demonstrated the ability of the technique on estimating the cyclic turbulence spectrum related to the periodic rotor wakes and the turbulence spectrum of the background flow. With these two spectra, the turbulence parameters of each domain could be successfully retrieved. One potential drawback of this approach is due to the cross-interference that might be experienced in the estimation of the Wigner–Ville spectrum (Antoni 2007). Despite the complexity of its implementation, the technique performs properly with experimental data. One particular issue reported in this work regarding the over estimation of the ILS is due to high power content in the low-frequency band of the turbulence spectrum. This sort of phenomenon is believed to not be turbulence related and can be filtered out from the turbulence spectrum by applying specific techniques as described in Mark (1981), Caldas et al. (2021).

Maunus et al. (2013) processed data from the SDT NASA test bed (Envia 2002). They observed that the ILS increases from hub to tip. Furthermore, these scales are larger for an axial position further downstream compared to one closer to the fan. They stated that, as previously reported by Podboy et al. (2003), this is due to the thickening of the wakes as they are convected with the stream. Maunus et al. (2013) argued that it is impossible to calculate passagewise distributions of the integral length scale with only hot-wire measurements. Instead, they estimated this length scale as a function of the root-mean-square velocity (in the streamwise direction), the mean energy dissipation rate per unit mass ε, and a Reynolds number dependent constant C_ε.

With the help of this formulation, the ILS could be estimated for the entire rotor passage. Results were compared with several RANS CFD simulations. The distribution of the ILS estimated from hot-wire data compared with several CFD was quite disparate and hard to draw any conclusion about possible trends.

Odier et al. (2018) analyzed hot-wire data obtained downstream of the fan, and the stator vanes of real turbofan engine (DGEN380). Results were compared with LES numerical computation. A separation of rotor wake and background turbulence was not performed in this study. A spatial distribution of turbulence integral time scale as well as turbulence intensity is shown from both experimental and simulation data.

Another possibility to estimate the turbulence parameters of rotor blade wakes is by using empiric methods. One to be cited is described by Moreau (2017). The estimation of the integral length scale is made based on the shape of the wake mean velocity. That means, no turbulence data is necessary; instead, the mean velocity profile of the wakes is used with help of some calibration factors to estimate the ILS. This method is particularly helpful for estimating turbulence parameters from simulation data, in the case when only the average profile of the flow downstream of the fan is available.

With that said, to the best of the author's knowledge, the only existing method to separate rotor wakes and background flow turbulence parameters from hot-wire data measured downstream of a rotor is the one presented by Jurdic et al. (2009). Different from this method, the new method proposed in our work is based in the time domain and use

data windows to separate the part of the turbulence signal corresponding to the rotor wake from the background flow. The duration and position in time of these windows are determined based on the cyclic variance of the turbulence signal, that means, the power of this signal as a function of the circumferential position. A threshold separates the two regions: low-variance is associated with the background flow, whereas high-variance to the rotor wakes. The proposed technique searches automatically the position and size of the data windows and separates both domains: rotor wakes and background flow. Overall, the proposed method can be applied to any signal to separate two superimposed processes, where one is cyclostationary and the other stationary. The requirement is that the processes have to have discernible variance.

3 Test rig and measurement setup

The data used in this work were measured by means of hot-wire anemometry in the fan test rig CRAFT. The CRAFT (Co-/ Counter Rotating Acoustic Fan Test rig) is a low-speed fan test rig, especially conceived for aeroacoustic and aerodynamic studies. The fan stage possesses an 18-bladed rotor and a 21-vaned stator, as shown in Figs. 1 and 2. The test rig can achieve fan speed up to 4500 RPM, 0.14 inlet Mach number with 0.48 blade tip Mach number. The design operating point of the baseline rotor–stator set is at $\eta = 4500$ RPM and flow coefficient of approx. $\phi = 0.33$. In order to establish homogeneous and low-turbulence levels at the fan inlet, an inflow control device (Caldas et al. 2022) is mounted onto the bellmouth, as shown in Fig. 3. A more detailed description of the test rig, the possible instrumentation and analyses capabilities are given by Tapken et al. (2021a,b).

The experiments are performed at corrected fan speeds. That means the actual fan speed in the experiment is slightly adjusted due to temperature changes to always produce the same blade tip Mach number as in a given reference. In this work, the reference used is the sea-level standard conditions: $T_{\mathrm{ref}} = 288.15\,K$ ($15°C$) and $p_{\mathrm{ref}} = 101,325$ Pa. The equation to compute the corrected speed η_{c} is given by:

$$\eta_{\mathrm{c}} = \eta\sqrt{\frac{T_{\mathrm{ref}}}{T_{\mathrm{t}}}}, \qquad [\mathrm{min}^{-1}] \tag{1}$$

where η is the measured fan speed during the experiment and T_{t} the inlet total temperature in K.

Different flow coefficients for a given fan speed are adjusted with the help of a conic throttle placed at the duct exhaust. The throttle position alters the open area at the duct exhaust, which alters the pressure drop at this location. As a consequence, the fan pressure ratio and axial flow speed

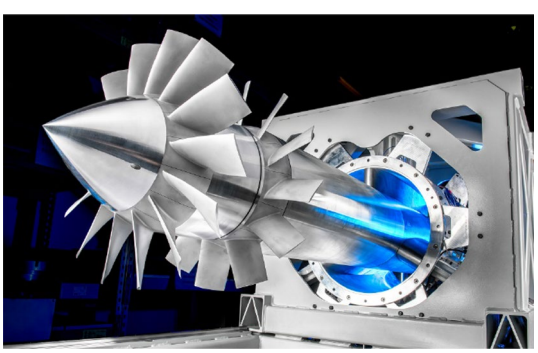

Fig. 1 Side view of the craft rotor without the outer casing. In this picture, the rotor–rotor configuration was photographed

Fig. 2 Front view of the rotor mounted in the duct. The ellipse shaped bellmouth is seen in white in the foreground

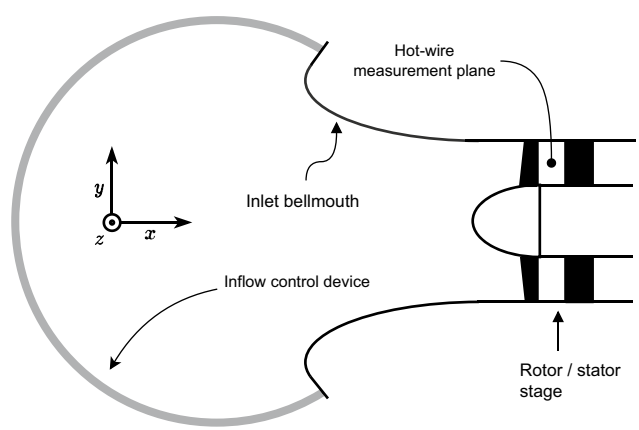

Fig. 3 Sketch of the hot-wire measurement setup. Measurement section is indicated downstream of the rotor and upstream of the stator vanes

are changed, allowing different axial flow speeds for a given constant fan speed. The flow coefficient is calculated via:

$$\phi = \frac{\overline{U}}{U_{\text{tip}}} = \frac{\overline{U}}{2\pi\omega R}, \tag{2}$$

where $\overline{U}$ is the inlet axial mean flow speed, U_{tip} is the tangential tip speed of the rotor, R the fan radius, and ω is the fan rotation speed in Hz.

The turbulence field downstream of the rotor was assessed by a hot-wire probe containing two tungsten wires (X-probe) of about 2.8 mm length and 9 µm in diameter (Meyer et al. 2019). With this setup, both the axial and circumferential velocity components are acquired. The probe was aligned with the expected exit flow angle in order to obtain an alignment of the probe and the flow downstream of the fan and avoid too high flow incidence angles with the hot-wire elements. With post-processing, these data are converted back to the machine coordinates. A digital low-pass filter is applied to the signal with cut-off frequency set to 40 kHz. A radial traverse was used to travel the probe inside the channel. For each measurement position 10 s of data were acquired sampled at $f_s = 192$ kHz. A one-pulse-per-rev trigger signal was also recorded to allow data resampling.

4 Separation of rotor wake and background turbulence parameters

Typically, the outcome data from a hot-wire measurement are referred to the machine coordinates. That means the velocity signals are referred to the axial $U(t)$, radial $V(t)$, and tangential $W(t)$ directions, as depicted in Fig. 4. Due to the swirl introduced by the fan in the flow, in the plane behind the fan the main stream is not anymore aligned with the axial line. As turbulence is modeled in terms of stream-wise (aligned with the flow) and transverse (orthogonal) velocity components, a coordinate transformation must be performed.

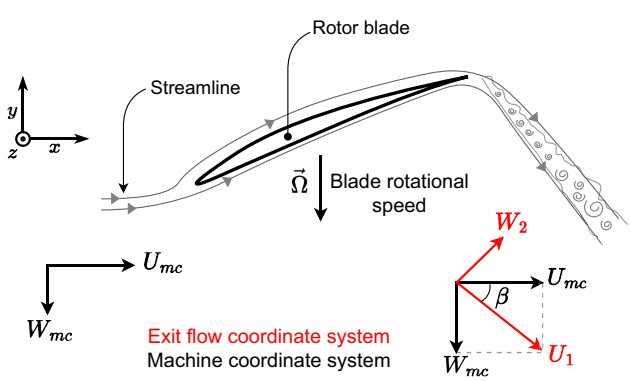

Fig. 4 Coordinate system used in the interstage section

The new reference frame for turbulence analysis considers the main stream-wise velocity component $U_1(t)$ and its respective transverse component $W_2(t)$, also known as the upwash velocity component. This last has by definition zero mean, as the stream-wise component $U_1(t)$ already consists of the vector sum $\mathbf{U}_1 = \mathbf{U}_{\text{mc}} + \mathbf{W}_{\text{mc}}$. $W_2(t)$ contains only the velocity fluctuations components that are transverse to the flow direction. The index "1" stands for the stream-wise component, whereas the index "2" for the transverse component. This is a common nomenclature in turbulence modeling. The exit flow angle in the rotor blade trailing edge β is calculated by:

$$\beta = \arctan\left(\frac{\overline{W}_{\text{mc}}}{\overline{U}_{\text{mc}}}\right), \tag{3}$$

where

$$\begin{aligned} U_{\text{mc}}(t) &= \overline{U}_{\text{mc}} + u(t) \\ W_{\text{mc}}(t) &= \overline{W}_{\text{mc}} + w(t), \end{aligned} \tag{4}$$

with

$$\overline{U}_{\text{mc}} = \mathbb{E}\{U_{\text{mc}}(t)\} = \lim_{T\to\infty} \frac{1}{T}\int_0^T U_{\text{mc}}(t)\mathrm{d}t, \tag{5}$$

where the operator $\mathbb{E}\{.\}$ denotes the expectation value. $u(t)$ and $w(t)$ refer to the zero mean stochastic component of each respective velocity component. $\overline{W}_{\text{mc}}$ is obtained identically as $\overline{U}_{\text{mc}}$ and therefore omitted for simplicity. Organizing the variables in a matrix form, and with the help of a coordinate transformation matrix, we obtain:

$$\begin{bmatrix} U_1(t) \\ W_2(t) \end{bmatrix} = \begin{bmatrix} \cos\beta & \sin\beta \\ -\sin\beta & \cos\beta \end{bmatrix} \begin{bmatrix} U_{\text{mc}}(t) \\ W_{\text{mc}}(t) \end{bmatrix} \tag{6}$$

and therefore

$$\begin{aligned} U_1(t) &= U_0 + u_1(t) \\ W_2(t) &= w_2(t) \\ \overline{U_1} &= U_0 \\ \overline{W_2} &= 0 \\ U_0^2 &= \overline{W}_{\text{mc}}^2 + \overline{U}_{\text{mc}}^2. \end{aligned} \tag{7}$$

As for illustration, Fig. 5 shows the velocity signals measured downstream of a rotating fan using hot-wire anemometry. More details about this technique will be given in the next chapters. The blade wakes are clearly seen in the periodic valleys of each signal. In total, 11 wakes are plotted. The black (axial direction) and red (circumferential direction) velocity components refer to the original machine

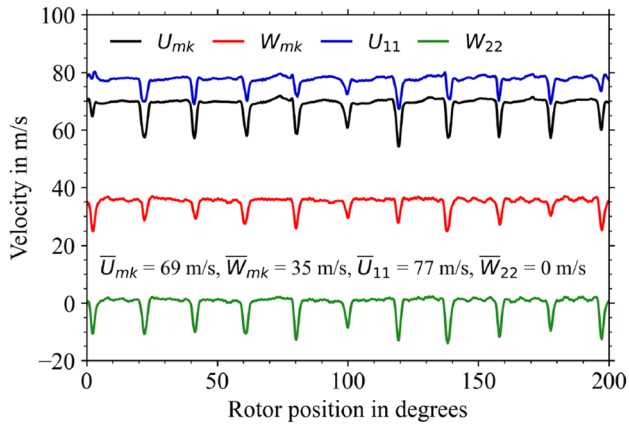

Fig. 5 Example of velocity signals measured downstream of the rotor. Black and red curves are in machine coordinates. Blue and green curves are in the new coordinate system. Mean values of each component are shown in the plot

coordinates system. The flow exit angle for this measurement point can be calculated by the resulting vector using the mean velocities displayed in the plot. For this case, with the help of Eq. 3, $\beta = 27°$. The resulting velocity signals after the coordinate system change are the longitudinal component, in blue, and the transverse component, in green. Note that $\overline{W}_{22} = 0$ m/s, as this is a transverse velocity component (perpendicular to the flow), but all the turbulent information is still present in the signal, that means, $\overline{w^2}_{22} > 0$ m^2/s^2.

4.1 New proposed technique based on measurement data

The newly implemented technique in this work is based on the separation of the rotor wake turbulence signal from the background turbulence signal measured downstream of a rotating fan. One way to look at this problem is by assuming that the turbulence data are a superimposition of two different processes: the periodic wakes coming from the rotor blades superimpose the background flow. Both processes when looked separately are assumed to be stationary. If a turbulence measurement could be performed inside a wake, that means, rotating with the rotor, the analysis of this signal would reveal a stationary process, similar to an airfoil's wake. However, as the measurement is performed in a static position and not rotating with the fan, the periodic incidence of the wakes on the measurement device (in our case the hot-wire anemometer) results in a cyclostationary signal. That means, a periodic snapshot of a stationary signal superimposes another stationary process.

The rotor wake turbulence has the characteristic of high-turbulence intensity, whereas the background flow discernible lower levels. The technique developed is based on separating the two processes by tapering the data (applying data windows in the signals). The two processes are divided based on a threshold applied to the cyclic variance signal, which represents the variance of the signal as function of the circumferential position. Figure 6 sketches the presented idea. On the left-hand side a synthetic turbulence signal similar to one measured downstream of a rotating fan is shown. In order to analyze the rotor wake signal, the region of the signal between the wakes (blue hatch, in the left-hand side plot in Fig. 6), referred to the background turbulence

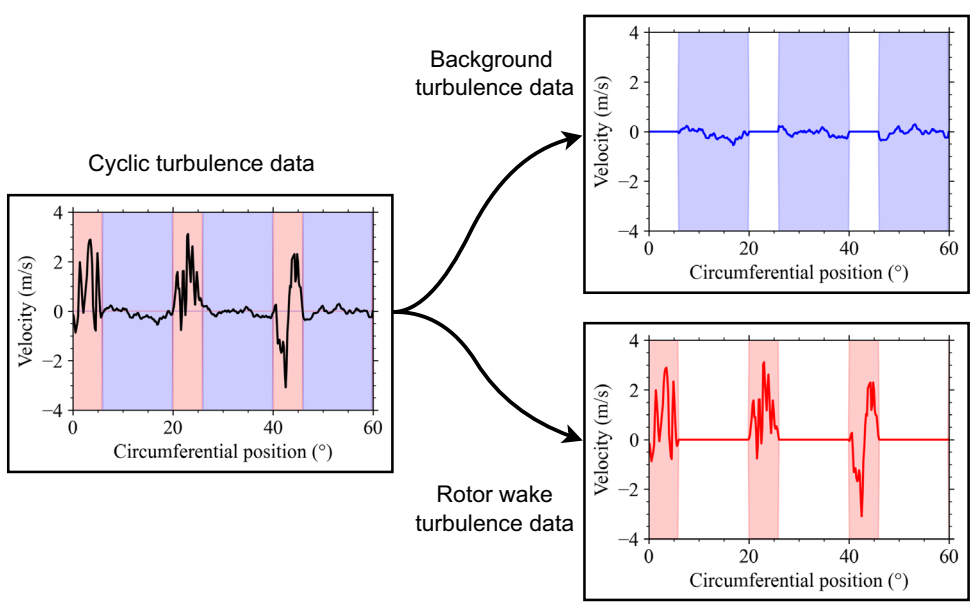

Fig. 6 Sketch of how the rotor wake - background turbulence separation technique works. Signals shown were obtained synthetically and represent only the turbulent fluctuations of each signal. The periodic mean fluctuations of the rotor wakes are not included in this signal

is multiplied by zero. The result is shown on the bottom-right hand side of this figure. This allows us to analyze the statistics of the wakes separately from the background flow. On the other hand, in order to investigate the background turbulence, the region of the signal corresponding to the rotor wakes is similarly multiplied by zero, as in the top-right-hand side of this figure. Evidently, the addition of these zeros implicates in a power loss of the signal. This power loss is along with the signal processing chain compensated.

The step by step of the technique is described as follows:

1. *Performing a cyclostationary analysis* The cyclostationary tool is used to separate the periodic velocity signal from the turbulence fluctuations. The signals $u_1(t)$ and $w_2(t)$ are already resampled and have an exact number of samples per revolution N_{rev}. For convenience, signals are organized as a 2D matrix with dimensions $n \times k$, where $n = 0, 1, \ldots, N_{\text{rev}} - 1$ is the sample position related to the angular position of the fan. $k = 0, 1, \ldots, K - 1$ is the kth revolution of the fan.

$$u_1(n,k) \triangleq u_1\left(\frac{nk}{f_s} + kT\right) \tag{8}$$

where T is the fan rotation period $T = 60/\eta$ in seconds and η the fan speed in RPM (revolutions per minute). The cyclic mean of the velocity signal, which can also be seen as the coherent part of the signal (CyS1—when performing a cyclostationary analysis) can be calculated by

$$\overline{u_1}(n) = \text{CyS1}\{u_1(n,k)\} = \frac{1}{K}\sum_{k=0}^{K-1} u_1(n,k). \tag{9}$$

On the other hand, the incoherent part of the signal—CyS2 (turbulent information)—resulting from the cyclostationary analysis is obtained by:

$$\begin{aligned} u_1'(n,k) &= \text{CyS2}\{u_1(n,k)\} \\ &= u_1(n,k) - \overline{u_1}(n) \quad \text{for } k = 0, 1, \ldots, K-1. \end{aligned} \tag{10}$$

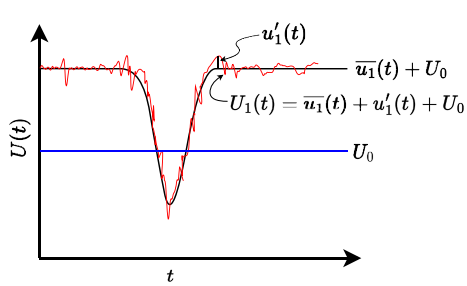

Fig. 7 Sketch of each constituent of an unsteady velocity signal measured downstream of a rotating fan

The best way to see the CyS2 signal is not as a vector in time, instead, as a $N_{\text{rev}} \times k$ matrix, which corresponds to a collection of time series vectors referring to each kth revolution of the fan. Figure 7 shows a representation of each of these velocity constituents. The blue curve represents the overall mean flow speed U_0. The black curve stands for the cyclic average $\overline{u_1}(t)$ added by the total mean speed U_0, where a typical blade wake shape is shown. The red curve illustrates $U_1(t)$, which is the sum of the stochastic oscillations $u_1'(t)$, the cyclic mean value $\overline{u_1}(t)$, and the overall mean U_0. The CyS2 component of the signal is represented by $u_1'(t)$ as the difference between the black and red curves.

2. *Calculating the cyclic variance of the signal* The cyclic variance refers to the variance of the turbulence as a function of the angular position. It can be easily calculated from $u_1'(n,k)$ by:

$$\begin{aligned} \text{Var}\{u_1(n,k)\} &= \overline{u_1}^2(n,k) - \overline{u_1}^2(n) \\ &= \frac{1}{K}\sum_{k=0}^{K-1}\left(u_1'(n,k)\right)^2. \end{aligned} \tag{11}$$

An example of a signal measured in the interstage of a fan is shown in Fig. 8. This data set shown was measured in the low-speed fan rig CRAFT, where the rotor blade count is $B = 18$, as shown in Sect. 3. The subsequent illustrations are also referred to this data set. In this figure, three fan revolutions $K = 3$ and three blade passages data $\theta = 60°$ or equivalently $n = 3N_b$ are shown. That means, the samples per blade

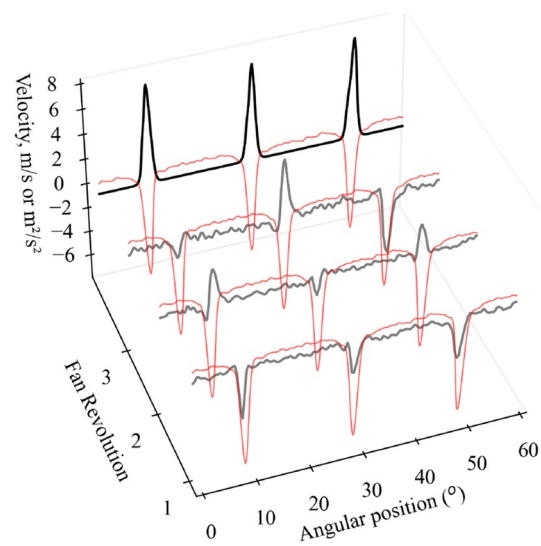

Fig. 8 Snapshot of the turbulence fluctuation signal $u_1'(n,k)$ for $k = 3$ fan revolutions in gray in m/s. Three blade passages are shown. The black curve shows the cyclic variance of $u_1(n,k)$ in m^2/s^2. The red curves show the periodic velocity mean $\overline{u_1}(n)$ in m/s.

passage is given by $N_b = N_{\text{rev}}/B = 113.8$ samples, for $N_{\text{rev}} = 2048$. The black curve in the back of this plot refers to the cyclic variance of the stream-wise velocity component. The gray curves are the instantaneous snapshots of the $u_1'(n,k)$ signal for $K = 3$ fan revolutions.

3. *Finding the center of the rotor wakes* Once the cyclic variance is calculated, it is necessary to determine where the center of the wakes is found. In other words, as in Fig. 8, regarding the black curve, how many samples separates the beginning of the signal $n = 0$ from the first peak of the cyclic variance signal, understood as the center of one rotor wake. The algorithm assumes that all wakes are equally spaced. Figure 9 top plot shows an example of a cyclic variance normalized by its maximum value. In order to find the center of the wakes, a train containing $B = 18$ impulses shaped with a Hann (see refs. Kay 1993; Percival and Walden 1993) window is firstly created. The Hann window is used as impulse shape for simplicity. Other impulse shapes could also be used. The window width is initially set to 30% of the width of a blade passage. The bottom plot of Fig. 9 illustrates a train of impulses for the case of $B = 18$ rotor blades. In this example, the first pulse is roughly at the first position $\theta = 0°$ or equivalently $n = 0$. The method works by multiplying the train of impulses by the cyclic variance signal, summing up the resulting signal and storing the output value. The train of impulses is then cyclic-shifted by one sample, and the same procedure is repeated. The algorithm performs this search N_b times, corresponding to one blade passage. This process can be mathematically described as follows. Firstly, one sample passage impulse $h(n, L)$ is defined by:

$$h(n,L) = \begin{cases} \text{Hann}(n) & \text{for } n = 0, 1, \ldots, L-1 \\ 0 & \text{for } n = L, \ldots, N_b - 1, \end{cases} \tag{12}$$

where L is the width of the impulse itself initially set as $L = 0.3N_b$. The train of impulses $I(n, n_\alpha, L)$ can be then defined as:

$$\begin{aligned} I(n, n_\alpha, L) &= h(n_b, L) z^{-n_\alpha} \\ n_b &= \text{mod}(n, N_b). \end{aligned} \tag{13}$$

The symbol z^{-1} used from the Z-transform ($z = j\omega$, and $j = \sqrt{-1}$) denotes the unit delay operator defined by $z^{-1}y(n) = y(n-1)$. Finally, a cost function $f(n_\alpha)$ is defined as a function of the sample shift n_α applied to the train of impulses and multiplied by the cyclic variance signal:

$$f(n_\alpha) = \sum_{n=0}^{N_{\text{rev}}} var\{u_1(n,k)\} I(n, n_\alpha, L), \tag{14}$$

and the sample corresponding to the distance from the beginning of the signal and the first wake center $n_{\alpha,c}$ is obtained by:

$$n_{\alpha,c} = \underset{n_\alpha \in [0, N_b]}{\text{argmax}}\ f(n_\alpha). \tag{15}$$

The cost function has typically a shape similar to a Gaussian curve. An example of this curve obtained from the signals shown in Fig. 9 is shown in Fig. 10. The x-axis refers to the rotor blade passage position, whereas the y-axis to the cost function normalized by its maximum. The advantage of this technique over, for example, searching for the peak in the cyclic variance signal, is the robustness introduced. This technique searches the strongest coherent structure with B peaks equally spaced in time. Any other structure, even with higher amplitude than the rotor wakes itself, would not bias the result. The only situation that can

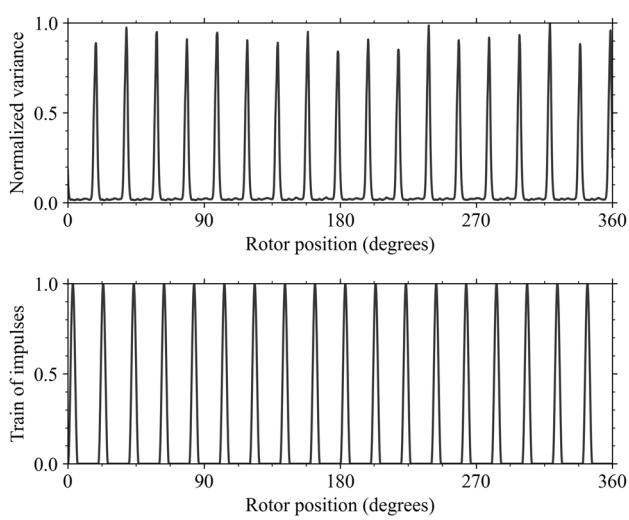

Fig. 9 Signals to be compared in order to find the rotor position. *Top:* Normalized cyclic variance as a function of rotor position. *Bottom:* Train of $B = 18$ equally spaced impulses. Impulses used have the Hann window shape

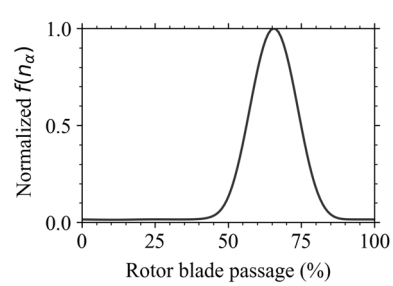

Fig. 10 Example of the cost function $f(n_\alpha)$ evaluated for the whole blade passage: $0 \le n_\alpha \le N_b$.

lead to deviation in the results is when a stronger structure with integer multiple of B peaks stronger than the rotor wakes is present in the signal. One example is the region close to the rotor blade tip. In this region, as shown later, tip vortices are present, which have B equally spaced peaks structure with power higher than blade wakes themselves. This problem can be overcomed by a technique discussed in the upcoming items.

4. *Estimating the average wakes amplitude* Once the position of the maximums in the cyclic variance vector is found, the average of these maximums is computed. This is done by averaging n_{avg} samples around the maximum of each blade passage. The default value used in this work is $n_{avg} = 3\%$ of N_b samples around the center of each rotor wake. In our case, ($N_{\text{rev}} = 2048$), this gives 3 samples. In other words, the average amplitude $\bar{A}_{u1}$ of the peaks in the signal $\text{var}\{u_1(n,k)\}$ is obtained by:

$$\bar{A}_{u1} = \sum_{n=0}^{N_{\text{rev}}-1} \text{var}\{u_1(n,k)\} I_2(n, n_{\alpha,c}, n_{avg}), \tag{16}$$

$$\bar{A}_{u1} = \frac{1}{n_{avg}B} \sum_{n=0}^{N_{\text{rev}}-1} \left[\text{var}\{u_1(n,k)\} \sum_{m=n_{\alpha,c}-(n_{avg}-1)/2}^{n_{\alpha,c}+(n_{avg}-1)/2} \delta(\text{mod}(n, N_b) - m) \right], \tag{17}$$

where $\delta(n)$ is the dirac-delta defined by:

$$\delta(n) = \begin{cases} 1 & \text{for } n = 0 \\ 0 & \text{else.} \end{cases} \tag{18}$$

In brief, in Eq. 17 the n_{avg} samples around each peak in the signal $\text{var}\{u_1(n,k)\}$ spaced by N_b are averaged.

5. *Estimating the wakes width* The width of the wakes L_w in samples is estimated by varying the width L of each impulse in the train of impulses $I(n, n_\alpha, L)$ and comparing it to the cyclic variance signal $\text{var}\{u_1(n,k)\}$. A cost function $g(L)$ of the impulse width L is defined as:

$$g(L) = \sum_{n=0}^{N_{\text{rev}}-1} \|\bar{A}_{u1} I(n, n_{\alpha,c}, L) - \text{var}\{u_1(n,k)\}\|$$
$$L_w = \underset{L \in [0, N_b]}{\text{argmin}}\, g(L), \tag{19}$$

where $\|\cdot\|$ stands for the absolute value operator. In other words, the optimal impulse width L_w is found when the width of the impulses in $\bar{A}_{u1} I(n, n_{\alpha,c}, L)$ gets as close as possible to the ones in the variance signal $\text{var}\{u_1(n,k)\}$, which results in a local minimum in this absolute difference. Figure 11 shows how the cost function $g(L)$ behaves as a function of L. In this plot, L is represented as a percentage of the rotor blade passage, as a way of normalizing the axis. In this case, the minimum value is found by approx. 33% of the blade passage. The width of the blade wakes $w_{w,k}$ is finally computed based on the train of impulses $I(n, n_{\alpha,c}, L_w)$ and a threshold value. $w_{w,k}$ is assumed to be the width of $h(n, L)^2$ in samples, when its amplitude drops by a specified threshold value relative to its maximum amplitude. In this work, this threshold is typically set between 90% and 95%.

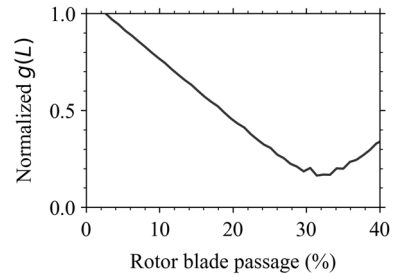

Fig. 11 Example of the cost function $g(L)$ evaluated for 40% of a blade passage: $0 \leq L \leq 0.4N_b$

6. *Generating the data tapers (windows)* Once the center of the rotor blade wakes and their width are known, the data tapers can be created in order to separate rotor wake and background turbulence data from $u_1'(n,k)$. Two types of tapers need to be created: one with a smooth window, for example, the Hann window, to indeed tape the data and avoid spectral leakage, for afterwards estimate the power spectral density, and another taper with a rectangular window. This second is used to compute the power present in the region delimited by the window. This power is used to correct the power loss introduced by the Hann windowing and the zeros between the windows. The N_{rev} long data tapers are defined as follows: The unsteady data is separated into blade wake signal $u_{1,w}(t)$ and background flow signal $u_{1,b}(t)$, where $t = nT_s$ and $T_s = 1/f_s$ is the sampling time. The separation is done by applying a suitable window in order to set to zero the values corresponding to the field outside of the region of interest. Similar to step 2 of this series of steps, two windows have to be generated in order to separate both signals. The window $H_w(n)$ is used to isolate $u_{1,w}(t)$, whereas $H_b(n)$ isolates $u_{1,b}(t)$. The rotor wakes smooth taper $H_w(n)$ is calculated as follows:

$$H_w(n) = h_w(n_b, w_w) z^{-n_\alpha},$$
$$h_w(n, w_w) = \begin{cases} \text{Hann}(n) & \text{for } n = 0, 1, \ldots, w_w - 1 \\ 0 & \text{for } n = w_w, \ldots, N_b - 1, \end{cases} \tag{20}$$

whereas for the background turbulence taper $H_b(n)$ it holds:

$$H_b(n) = h_b(n_b, w_w)z^{-n_a},$$
$$h_b(n, w_w) = \begin{cases} 0 & \text{for } n = 0, 1, \dots, w_w - 1 \\ \text{Hann}(n) & \text{for } n = w_w, \dots, N_b - 1, \end{cases} \quad (21)$$

$n_b = \text{mod}(n, N_b)$. The rectangle windows $R_w(n)$ and $R_b(n)$ are obtained similarly by:

$$R_w(n) = \text{rect}_w(n_b, w_w)z^{-n_a},$$
$$\text{rect}_w(n, w_w) = \begin{cases} 1 & \text{for } n = 0, 1, \dots, w_w - 1 \\ 0 & \text{for } n = w_w, \dots, N_b - 1, \end{cases} \quad (22)$$

whereas for the background turbulence it holds:

$$R_b(n) = \text{rect}_b(n_b, w_w)z^{-n_a},$$
$$\text{rect}_b(n, w_w) = \begin{cases} 0 & \text{for } n = 0, 1, \dots, w_w - 1 \\ 1 & \text{for } n = w_w, \dots, N_b - 1. \end{cases} \quad (23)$$

7. *Separating background and wake data* With the tapers available, the separated signals can be obtained by:

$$\begin{aligned} u'_{1,w}(n) &= H_w(\text{mod}(n, N_{\text{rev}}))u'_1(\text{mod}(n, N_{\text{rev}}), k), \\ u'_{1,b}(n) &= H_b(\text{mod}(n, N_{\text{rev}}))u'_1(\text{mod}(n, N_{\text{rev}}), k), \\ k &= \lfloor \frac{n}{N_{\text{rev}}} \rfloor, \end{aligned} \quad (24)$$

where k now is obtained by the integer division of n by N_{rev} with the operator $\lfloor . \rfloor$. $u'_{1,w}$ stands for the rotor wake signal and $u'_{1,b}$ for the background turbulence signal. At this stage, the signals do not need to be organized in a matrix fashion anymore, instead, as vectors. With the signals separated, the only missing step is to correct their energy loss, as shown in the next steps.

8. *Computing the original energy of each component* The power of rotor wake signal σ_w^2 and the background turbulence signal σ_b^2 are calculated by:

$$\sigma_w^2 = \frac{1}{w_w BK} \sum_{n=0}^{N_{\text{rev}}-1} \sum_{k=0}^{K-1} \left[R_w(n) u'_1(n, k) \right]^2, \quad (25)$$

and similarly, for the background turbulence:

$$\sigma_b^2 = \frac{1}{w_w BK} \sum_{n=0}^{N_{\text{rev}}-1} \sum_{k=0}^{K-1} \left[R_b(n) u'_1(n, k) \right]^2, \quad (26)$$

as both are already zero-mean signals.

9. *Computing the power spectral density* The biased power spectral density (signal power loss not yet corrected) of the rotor wakes is obtained by $\hat{S}_{11,w}(f_n)$:

$$\hat{S}_{11,w}(f_n) = \left[\mathcal{F}\{u'_{1,w}(n)\} \right]^2, \quad (27)$$

where $\mathcal{F}\{.\}$ stands for the discrete Fourier transform, and f_n the discrete frequency bin. For simplicity, the power spectral density estimation is in this text expressed as the squared value of the Fourier transform of the signal. However, in practice the Welch method should be used to improve estimation performance. The bias of the power spectral density can be corrected as follows:

$$S_{11,w}(f_n) = \sigma_w^2 \frac{\hat{S}_{11,w}(f_n)}{\Delta f_n \sum_{f_n} \hat{S}_{11,w}(f_n)}. \quad (28)$$

The dividing term in this equation is essentially the power of the spectrum $\hat{S}_{11,w}(f_n)$. This division normalizes the spectrum so that its power is equal to the unity. Δf_n stands for the discrete frequency resolution. The normalized spectrum is then corrected with the term σ_w^2 to adjust it to the correct power. The power spectral density of the background turbulence $S_{11,b}(f_n)$ is obtained in the same way by:

$$\begin{aligned} \hat{S}_{11,b}(f_n) &= \left[\mathcal{F}\{u'_{1,b}(n)\} \right]^2 \\ S_{11,b}(f_n) &= \sigma_b^2 \frac{\hat{S}_{11,b}(f_n)}{\Delta f_n \sum_{f_n} \hat{S}_{11,b}(f_n)}. \end{aligned} \quad (29)$$

For the other transverse velocity components such as the w_2, the data tapers used are the same as used for the u_1 component. Step 1 needs to be repeated in order to obtain the cyclostationary components. After that, steps from 2 to 6 should be skipped, jumping straight to step 7 until step 9.

10. *Estimating turbulence parameters from the PSD* After the estimation of the PSD of each spatial domain, the turbulence parameters of interest: turbulence intensity and integral length scale needs to be estimated. The turbulence intensity is estimated by

$$T_x = \frac{\sqrt{\sigma_x^2}}{U_0}, \quad (30)$$

where σ_x^2 is the variance of signal and U_0 the mean longitudinal velocity at that measurement position. The turbulence integral length scale on the other hand can be estimated from the PSD of the velocity signal S_{xx} under the Taylor assumption or "frozen turbulence" (Pope 2000) by

$$\Lambda = \frac{S_{xx}(0)U_0}{2\sigma_x^2}, \quad (31)$$

which holds for both longitudinal and transverse velocity components. No isotropy assumption is

assumed by using this equation. If HIT is assumed, however, the estimator for the integral length scale gains some degree of robustness by allowing an average in the low-frequency band of the velocity PSD. The equation to compute it from the longitudinal velocity PSD is given by

$$\Lambda_1 = \frac{U_0}{4\sigma_u^2 \Delta f} \int_0^{\Delta f} S_{uu}(f)\mathrm{d}f, \tag{32}$$

where Δf is the frequency band used to average the PSD. Values to be used depend on the frequency band of the PSD, where the it starts to roll-off. Typical values for low-speed aerodynamics lie in 80 Hz < Δf < 200 Hz. The ILS can also be obtained from the transverse velocity component PSD as:

$$\Lambda_2 = \frac{U_0}{2\sigma_w^2 \Delta f} \int_0^{\Delta f} S_{ww}(f)\mathrm{d}f. \tag{33}$$

The robustness of this estimator is considerably higher than the one from Eq. 31, suffering less influence from the spectral estimation parameters. In this work, Eqs. 32 and 33 are used to compute the integral length scale of each respective velocity component. More details on the performance of each estimator are found in Caldas et al. (2021).

11. *Increasing the robustness of the algorithm* Turbulence data measured downstream of a rotor is not always clean from secondary phenomenon taking place. In other words, turbulence data may contain additional effects other than the rotor wakes. A typical example is the blade tip vortex present in measurement points performed close to the rotor outer casing. This is due to flow leakage in the gap between blade and duct wall. The cyclic variance of the turbulence fluctuations at this region (tip vortex) is often higher than the variance of the rotor wakes themselves. Figure 12 shows an example of a measurement performed at radial position respective to 95% of the blade span (4 *mm* away from the duct wall). In this figure, the peaks with variance of about 7.5 m^2/s^2 are due to the blade wakes, whereas the strong peaks with variance > 30 m^2/s^2 are due to the blade tip vortex. If the presented algorithm is applied to these data, the peaks associated with the tip vortex would be detectable as the blade wakes, due to their higher power. In this work, all region outside the blade wake is classified as background turbulence, which includes blade tip vortex. In order to guide the algorithm to not detect tip vortex as blade wakes, the following can be done: for a set of radial measurement positions ranging from blade tip to root, the algorithm has to start the wake detection at some radial position close to the blade mid-span, where the flow is often clean and free of secondary effects. Knowing the position and width of the wakes with respect to the trigger signal, the algorithm can move to the next radial position in the direction to the blade tip (duct wall) and afterwards to the blade root (hub). The position and width of the wakes with respect to the previous processed radial position have to be in a range pre-defined by the user, which works as constraints for algorithm. For example, if for a given radial position, the first blade wake was detected at 20° and the angle difference allowed between radial positions is set by 1.5°, the wake position of the next radial measurement position shall be scanned and found only in the range of 20 ± 1.5°. This procedure is based on the physics of the flow itself, as the blade wake position in the data from a radial position cannot be found several degrees apart from the previous measured radial position. An exemplary result that shows the detected wake region and the blade tip vortex is depicted in Fig. 13. The

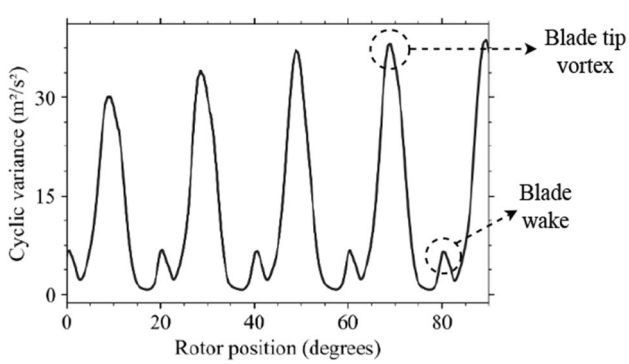

Fig. 12 Cyclic variance at the radial position respective to 95% of the blade span (4 mm away from the duct wall). 4.5 blade passages are shown. Peaks associated with the blade tip vortices and blade wakes are indicated

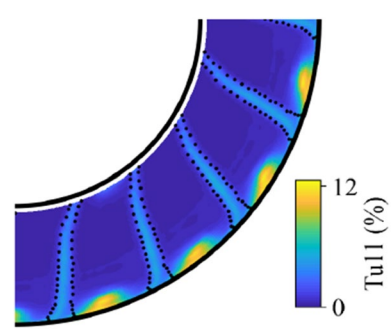

Fig. 13 Turbulence intensity distribution for the longitudinal velocity component. Tip vortices have the highest turbulence grades. Automatic detected wake areas are shown with blade dots. Fan operating point: η_c = 4500 RPM, ϕ = 0.33

black dots represent where the borders between what is considered rotor wake and background flow lie. This figure shows the turbulence intensity distribution of the longitudinal velocity component as function of radial and circumferential positions.

5 Experimental results

Data were selected for a constant fan speed of $\eta_c = 4500$ RPM and three different flow coefficients: $\phi = [0.40, 0.33, 0.28]$. This produces an inlet Mach number flow velocity of approx. $M_{inlet} = [0.12, 0.10, 0.087]$, respectively. For $\phi = 0.40$, the fan produces very low total pressure rise and works more as a ventilator than as a compressor. The design point of this rotor–stator set is, as discussed in Sect. 3, at $\eta = 4500$ RPM and $\phi = 0.33$ (approx.). It was observed experimentally that this fan stalls at $\phi \approx 0.26$ with the given ambient conditions.

Figure 14 displays the estimated PSD of the longitudinal velocity component measured at two radial positions and two fan operating points. The top plots refer to a measurement point at 7 mm (92% of blade span) away from the outer casing. At this position, the background turbulence (blue curve) levels are high due to the blade tip vortex. These values are even higher than the blade wake turbulence (red curve) itself. The black curve shows the PSD of the unsteady velocity signal before the technique has been applied. Tones are present in this PSD due to the periodic fluctuations associated with the velocity deficit from the rotor wakes, which are still present in this signal. These periodic components are displayed in red in Fig. 8. Comparing the left-hand top plot to the right-hand top plot ($\phi = 0.40$ vs. $\phi = 0.28$, respectively, both at $\eta_c = 4500$ RPM), virtually no difference is observed in the PSD level of the background flow. A higher incidence of tones is, however, seen for the higher flow coefficient case (left plot). For the wake turbulence, however, the PSD levels shifts slightly up and to the right, which means an increase in the turbulence levels and a slight decrease in the integral length scale.

The bottom plots in Fig. 14 refer to a measurement position at 36 mm away from the outer casing (59% of blade span), roughly at mid blade span. At this measurement position, the background turbulence levels are much lower compared to the total signal measured and the wake turbulence, as most of the variance measured is due to the rotor wakes. A noticeable increase in the wake turbulence levels is again observed for an increase in blade loading (reduction in flow coefficient). The background turbulence levels do not change considerably between these two operating points.

Figure 15 shows the average velocity of the longitudinal velocity component for the constant fan speed of $\eta_c = 4500$ RPM and for the three flow coefficients measured. The black dots illustrate where the automaticly detected border between blade wakes and background flow lies. A better view of this border will be given in the next figures. The $B = 18$ radially distributed velocity deficit pattern associated with the rotor wakes in light blue color is clear in all

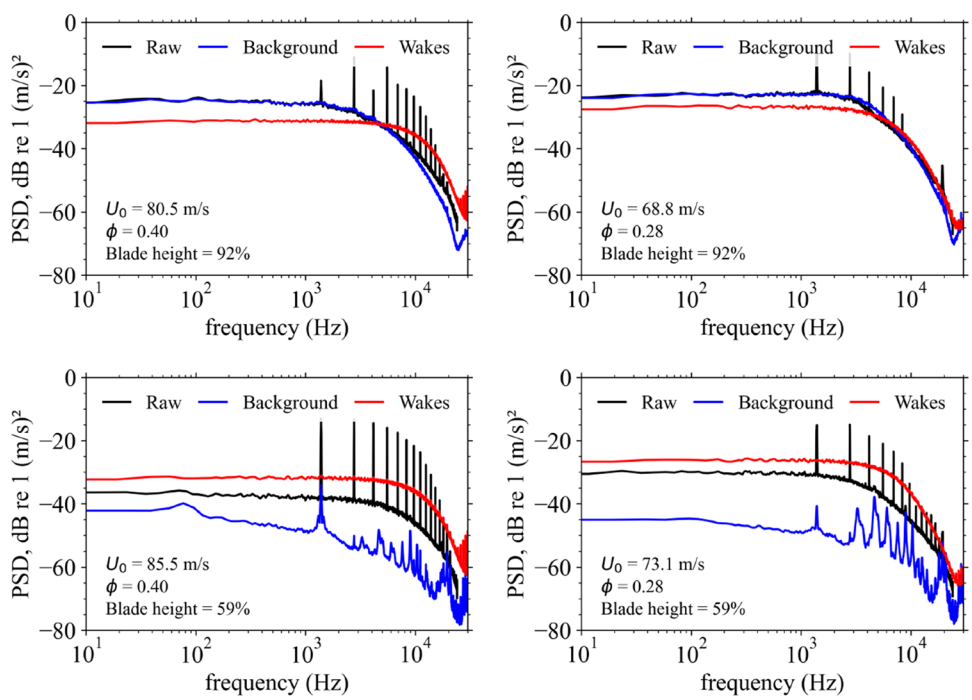

Fig. 14 PSD of the longitudinal velocity component of the raw signal (black), separated blade wakes (red), and background flow (blue). *Top* and *bottom:* Measurement points at 7 mm and 36 mm away from the outer casing (92% and 59% of blade span), respectively. *Left:* $\phi = 0.40$ and *right:* $\phi = 0.28$. All plots refer to the fan speed of $\eta_c = 4500$ RPM

plots. The green-yellow color between the rotor wakes represents the background flow, or the free-stream. A higher flow speed is observed in the region around the inner casing (fan hub). The reason for that is not fully understood. A deficit of velocity is also found in the region close to the outer casing, associated with its boundary layer and the blade tip vortex. Both the wake thickness and the tip vortex thickness are proportional to the blade loading, or inversely proportional to the flow coefficient.

Figure 16 displays the turbulence intensity distribution of the longitudinal velocity component U_1 for the same fan operating points. In these plots, the low-turbulence level area (dark blue) associated with the background flow is clearly distinguishable from the rotor wakes turbulence (light blue). The blades tip vortex (yellow spots near the outer casing and between every blade wake) is responsible for generating the highest turbulence levels measured. In this figure, the thickening of the tip vortex and blade wakes with the increase

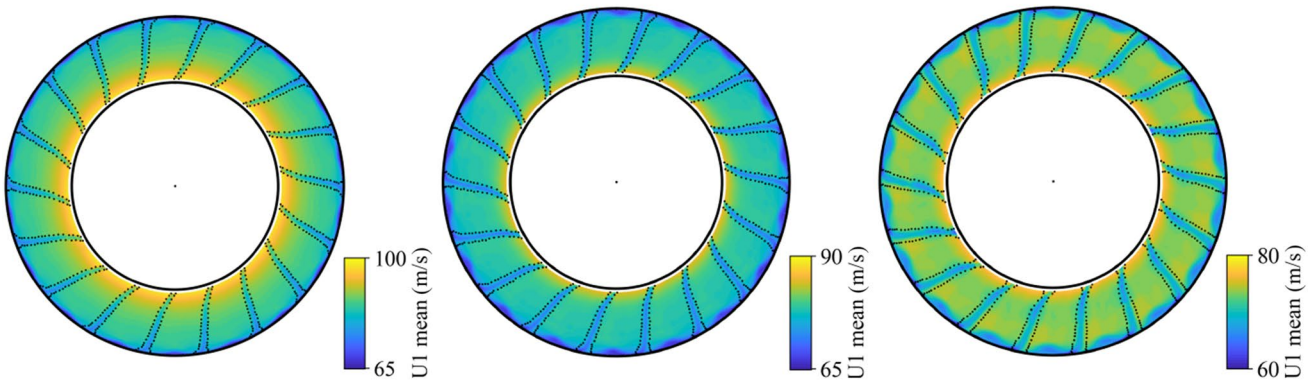

Fig. 15 Average speed of the longitudinal velocity component U_1. Fan operating point: η_c = 4500 RPM. *Left:* $\phi = 0.40$, *middle:* $\phi = 0.33$, and *right:* $\phi = 0.28$

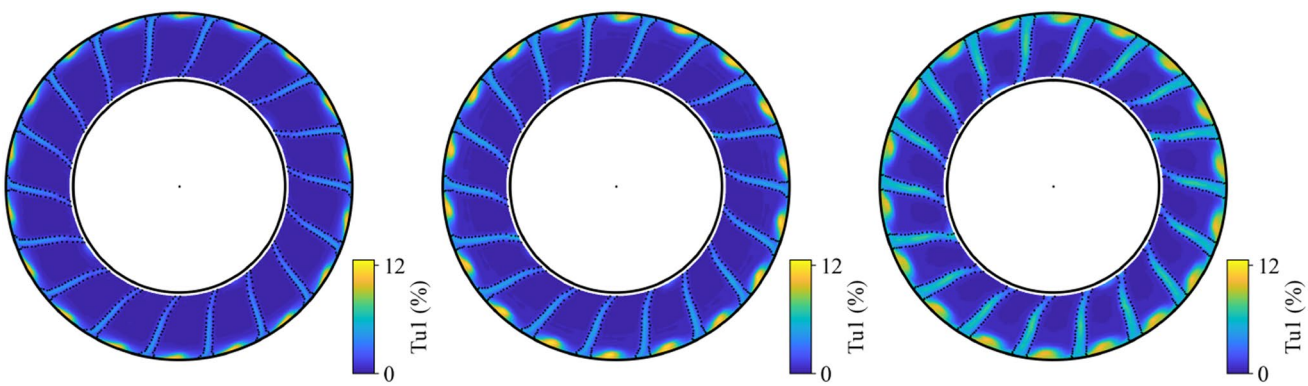

Fig. 16 Turbulence intensity of the longitudinal velocity component U_1. Fan operating point: η_c = 4500 RPM. *Left:* $\phi = 0.40$, *middle:* $\phi = 0.33$, and *right:* $\phi = 0.28$.

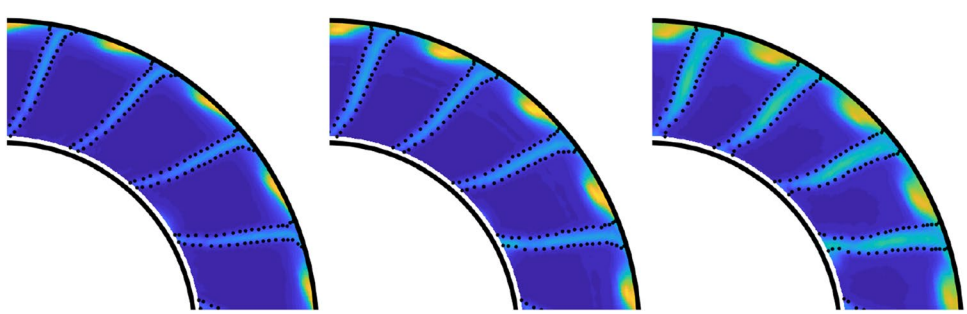

Fig. 17 Closeup in the top-right quarter of each plot of Fig. 16

in blade loading is more evident. A closer look in the top-right quarter of each of these plots is shown in Fig. 17. In this figure, the black dots representing the detected border between blade wake and background flow are more discernible. Furthermore, the progressive change in wake thickness as well as the tip vortex are better visualized. Interestingly, the turbulence intensity of the tip vortex seems to reach the highest values for $\phi = 0.33$, and not for $\phi = 0.28$ with the highest blade loading.

Figure 18 shows the turbulence distribution of the transverse velocity component W_2 for the same fan operating points. The color mapping scale was kept the same (from 0 to 12%). Slightly lower turbulence levels are observed in the wake region. The tip vortex for this velocity component also shows lower turbulence intensity values compared to the longitudinal component.

The distribution of the turbulence intensity as a function of the blade height is shown in Fig. 19. Both the rotor wakes and the background flow parameters are shown for the two velocity components U_1 and W_2. The curves represent an average of the turbulence intensity of either all blade wakes, or of the background flow for each radial position measured. No noticeable difference is observed between the two fan operating points $\phi = 0.40$ and $\phi = 0.33$ in these plots. The increase in the tip vortex is, however, observed in the blue curves referred to the background flow. Outside this region, the background flow has roughly same turbulence intensity numbers, which is one requirement (among others) for flow isotropy. The same does not hold for the blade wake. Inside the rotor blade wakes, the longitudinal velocity component seems to have almost double the levels of turbulence intensity than the transverse one. The blade wakes properties did not change considerably between these two fan operating points.

For $\phi = 0.28$, however, besides the further growth of the tip vortex area, an overall increase in the turbulence intensity of the blade wakes over the whole blade span is observed. This result agrees with the observations from Evans (1975). A possible reason for that is that the suction side of the blades is near reaching stall, which happens at approx. $\phi = 0.26$. The lower the flow coefficient (i.e., higher blade loading) is, the closer to the leading edge the boundary layer transition from laminar to turbulent occurs in the blade suction side. Along with that, in this condition flow separation can also occur at the blade trailing edge. A pronounced increase at 50% of blade height is noticed for the

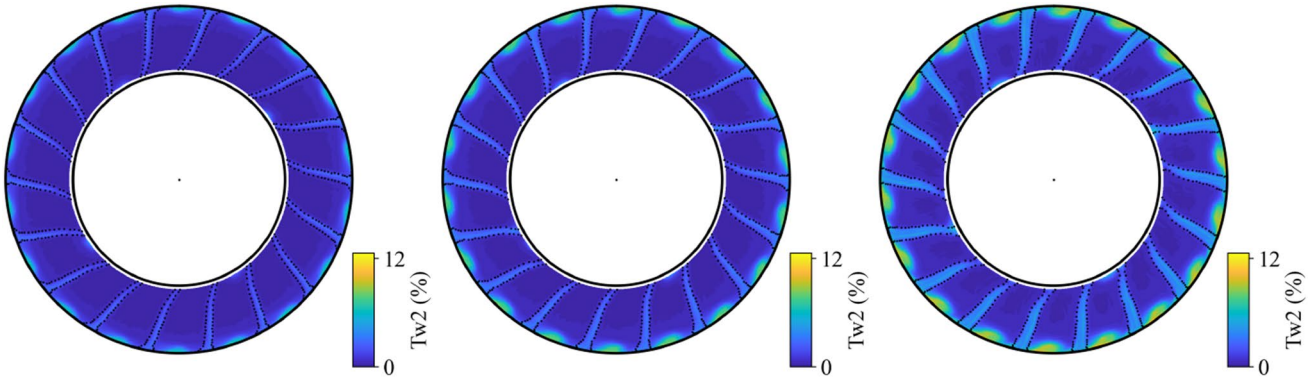

Fig. 18 Turbulence intensity of the transverse velocity component W_2. Fan operating point: $\eta_c = 4500$ RPM. *Left:* $\phi = 0.40$, *middle:* $\phi = 0.33$, and *right:* $\phi = 0.28$

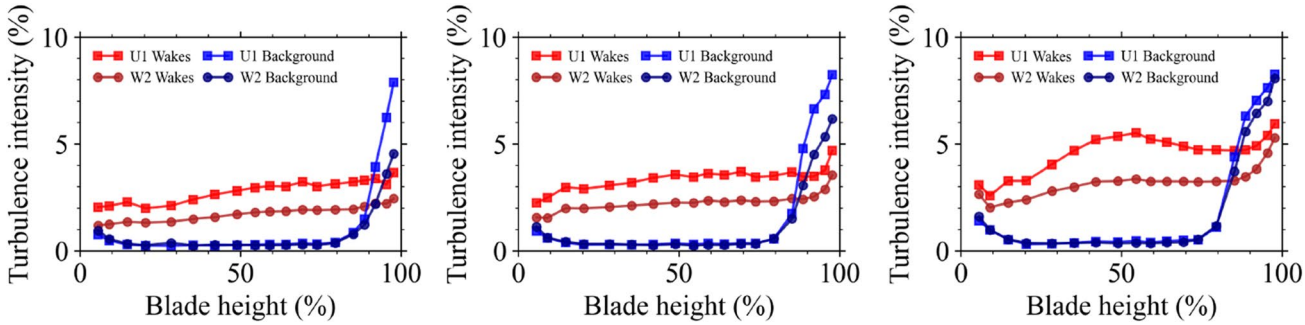

Fig. 19 Radial distribution of the turbulence intensity of both rotor wakes and background flow. Both velocity components are displayed U_1 and W_2. Fan operating point: $\eta_c = 4500$ RPM. *Left:* $\phi = 0.40$, *middle:* $\phi = 0.33$, and *right:* $\phi = 0.28$

longitudinal component. This can be a hint of the first region of the blade to enter in stall condition, when the flow coefficient continues to shrink.

The distribution of the turbulence integral length scale normalized by the blade chord length $C = 62$ mm as a function of blade height is shown in Fig. 20. Again, both the rotor wakes and the background flow parameters are shown for both velocity components U_1 and W_2. The ILS of the rotor wakes decreases slightly with the increase in blade loading. The values stay in the range of approx. 3–7% of the blade chord length. The difference in values for both velocity components of the rotor wakes seems to reduce with increase in blade loading. The transverse velocity component has higher values compared to the longitudinal one. This is opposite as observed for the turbulence intensity in Fig. 19, where the longitudinal component always showed greater values than the transverse one. At this point, the wake turbulence seems to have more energy in the longitudinal direction and shorter integral length scale compared to the transverse direction.

Two peaks are observed for the radial positions close to the hub and the outer casing for the dark blue curves of Fig. 20, referring to the transverse velocity component of the background flow. This is observed for all three flow coefficients. A hypothesis is that these peaks are associated with the two wall boundary layers: fan hub and outer casing. The ILS values of the background flow seem to reduce with increasing blade loading, especially for the longitudinal velocity component.

In order to get an overview of each parameter as a function of the flow coefficient, an average over the measured span was calculated using:

$$\overline{x} = \int_{r_1}^{r_2} x(r)\mathrm{d}r/(r_2 - r_1), \tag{34}$$

where r is the measurement radial position and $x(r)$ is either the turbulence intensity or the integral length scale as a function of the radial position. r_1 and r_2 stand for the first and last evaluated radial positions. The average values for each flow coefficient are shown in Fig. 21, in addition to the flow coefficients 0.30 and 0.36. In this figure, the trends are clearer for both turbulence intensity and integral length scale. The increase in blade loading (reduction in flow coefficient) resulted in an increase in the turbulence intensity of both velocity components, as well as in both rotor wakes and background flow regions. The increase in the turbulence intensity of the background flow, less preeminent than for the rotor wakes, is likely due to the increase of the rotor tip vortex effect.

For the integral length scale, however, different trends are observed. The increase in blade loading increased the average values of the length scales of the rotor wakes, what is

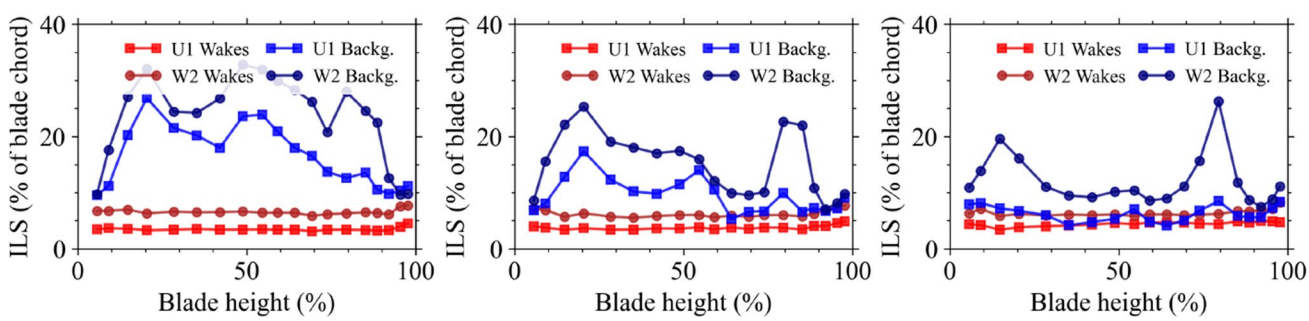

Fig. 20 Radial distribution of the integral length scale of both rotor wakes and background flow. Values are normalized by the blade chord length $C = 62$ mm. Both velocity components are displayed U_1 and W_2. Fan operating point: $\eta_c = 4500$ RPM. *Left:* $\phi = 0.40$, *middle:* $\phi = 0.33$, and *right:* $\phi = 0.28$

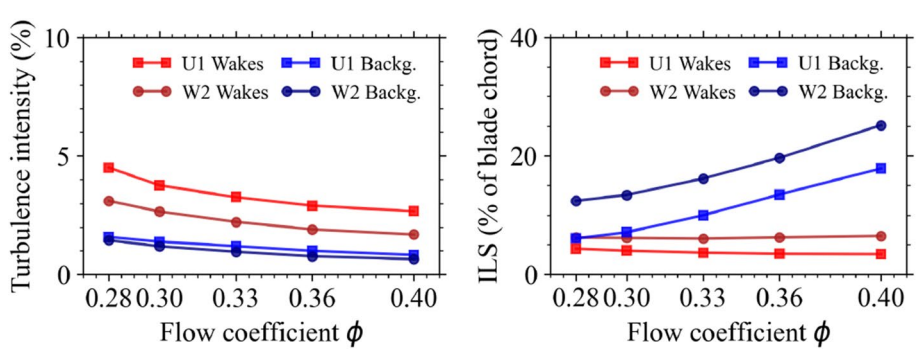

Fig. 21 Average values of the turbulence intensity (left plot) and of the integral length scale (right plot) over the blade span for three different flow coefficients. Fan speed: $\eta_c = 4500$ RPM

believed to be due to the widening of the rotor wakes. However, the opposite was observed for the background flow. The reason for this phenomenon is not well understood by the authors. One hypothesis is the inverse relationship of the length scales with the signal variance as shown in Eq. 31, as the variance increases with the increase in blade loading. Another hypothesis is its dependence with the average flow speed.

6 Conclusions

A new technique for the separation of turbulence parameters such as turbulence intensity (or variance, or turbulent kinetic energy) and integral length scale from rotor wakes and background flow was proposed. The technique works in time domain and is suitable for turbulence velocity data measured in discrete positions downstream of a rotating fan, such as from hot-wire anemometry. The technique uses the cyclic variance of the unsteady velocity signal as input parameter to determine the two region domains: blade wake and background flow. By applying suitable data tapers in the signal, the two processes are sorted out: blade wakes and background turbulence flow.

Data from a low-speed test rig validated the developed algorithm. Its robustness also allowed the separation of blade tip vortex from the rotor wakes. Results agree with the literature references found. The width of the wakes and the tip vortex region increase with the blade loading. For the highest fan loading analyzed, a significant increase in the rotor wake turbulence intensity was observed. The turbulence intensity of the longitudinal component of the wake was always considerably higher than the transverse component, suggesting flow anisotropy.

The radial profile of the turbulence integral length scale of the rotor wakes did not change considerably among the three analyzed flow coefficients. For the background flow, however, a consistent decrease of the ILS values was observed with the reduction in flow coefficient. Two peaks were identified for all flow coefficients in the background flow for the transverse velocity component. One hypothesis is that they are associated with the hub and outer casing boundary layer.

Acknowledgements The authors would like to thank all the DLR colleagues involved directly and indirectly in the preparation of the CRAFT test rig for measurements, in performing the measurements, and discussing results. A special acknowledgment is given to the workshop colleagues Sebastian Kruck, Oliver Klose and Angelo Rudolphi, who make the CRAFT test rig ready for measurements, and to Lukas Kähn for his support with the hot-wire measurements.

Author contributions All authors contributed to the study conception and design. Material preparation, data collection, and analysis were performed by LC and RM. The first draft of the manuscript was written by LC and all authors commented on previous versions of the manuscript.

Funding Open Access funding enabled and organized by Projekt DEAL. Not applicable.

Data availability Not applicable.

Code availability Not applicable.

Declarations

Conflict of interest The author's declared that they have no conflict of interest.

Ethics approval Not applicable.

Consent to participate Yes.

Consent for publication Yes.

References

Airbus (2003) Getting to grips with aircraft noise. Technical report, Airbus S.A.S

Antoni J (2007) Cyclic spectral analysis in practice. Mech Syst Signal Process 21:597–630

Astley RJ, Agarwal A, Joseph PF, et al (2007) Predicting and reducing aircraft noise. In: 14th international congress on sound and vibration, airns, Australia

Caldas L, Kissner C, Behn M et al (2021) Comparison of techniques for the estimation of flow parameters of fan inflow turbulence from noisy hot-wire data. Fluids 6(11):372 (https://www.mdpi.com/2311-5521/6/11/372)

Caldas L, Kruck S, Klähn L et al (2022) Construction and assessment of an inflow-control-device for a low-speed aeroacoustic fan rig. AIAA J 60(9):5299–5312. https://doi.org/10.2514/1.J061729

Camp TR, Shin HW (1995) Turbulence intensity and length scale measurements in multistage compressors. J Turbomach 117(1):38–46

Envia E (2002) Souce diagnostic test-vane unsteady pressure results. Technical report, NASA, Technical Report No. TM-2002-211808

Envia E (2018) Noise emissions from commercial aircraft. Green aviation: reduction of environmental impact through aircraft technology and alternative fuels CRC Press, pp 3–24

Evans RL (1975) Turbulence and unsteadiness measurements downstream of a moving blade row. J Eng Power 97(1):131–139

Giannakis GB, Madisetti VK, Williams DB (1998) Digital signal processing handbook. CRC Press, Boca Raton, FL, chap Cyclostationary signal analysis

Hinze JO, Clark BJ (1975) Turbulence. McGraw-Hill series in mechanical engineering

Jurdic V, Joseph P, Antoni J (2009) Investigation of rotor wake turbulence through cyclostationary spectral analysis. AIAA J 47(9):2022–2030

Kay SM (1993) Fundamentals of statistical signal processing. Prentice Hall PTR

Kholodov P, Koch R, Sanjosé M, et al (2021) Wall-resolved large eddy simulation of a realistic turbofan rotor for noise prediction. In: AIAA aviation forum, Online, AIAA 2021-2256, pp 2–6

Lengyel-Kampmann T, Bischoff A, Meyer R, et al (2012) Design of an economical counter rotating fan: comparison of the calculated and measured steady and unsteady results. In: Turbo Expo: Power for Land, Sea, and Air. Vol. 44670. American Society of Mechanical Engineers

Lewalle J, Ashpis. DE (2004) Estimation of time scales in unsteady flows in a turbomachinery rig. Tech. rep., NASA/TM-2004-209452

Lewis D, Moreau S, Jacob M (2020) Broadband noise predictions on the acat1 fan stage using large eddy simulations and analytical models. In: 26th AIAA/CEAS aeroacoustics conference, virtual

Mark WD (1981) Characterization, parameter estimation, and aircraft response statistics of atmospheric turbulence. NASA contractor report 3463

Maunus J, Grace S, Sondak D et al (2013) Characteristics of turbulencein a turbofan stage. J Turbomach 135(2):021024

Meillard L, Schnell R, Meyer R, et al (2013) Time resolved pressure and velocity measurements at the dlr uhbr-fan and comparison with simulation data. In: 62. Deutscher Luft- und Raumfahrtkongress, Stuttgart, Germany, pp 10–12

Meyer R, Knobloch K, Hakansson S (2015) Hot-wire measurement in a direct driven high speed turbo fan (ddtf) rig. In: ETC-11-256. 11th European turbomachinery conference, Madrid, Spain, pp 23–27

Meyer R, Hakansson S, Hage W, et al (2019) Instantaneous flow field measurements in the interstage section between a fan and the outlet guiding vanes at different axial positions. In: Proceedings of the 13th European conference on turbomachinery fluid dynamics and thermodynamics, Lausanne, Switzerland., http://www.euroturbo.eu/paper/ETC2019-330.pdf

Moreau A (2017) A unified analytical approach for the acoustic conceptual design of fans of modern aero-engines. PhD thesis, Technische Universität Berlin

Odier N, Duchaine F, Gicquel L, et al (2018) Evaluation of integral turbulene scale through the fan stage of a turbofan using hot wire anemometry and large eddy simulation. In: Proceedings of ASME Turbo Expo 2018, turbomachinery technical conference and exposition, GT2018, Oslo, Norway, pp 11–15

Percival DB, Walden AT (1993) Spectral analysis for physical applications. Cambridge University Press

Podboy GG, Krupar MJ, Helland SM, et al (2003) Steady and unsteady flow field measurements within a nasa 22-inch fan model. Technical report, NASA, Technical Report No. TM-2003-212329

Pope SB (2000) Turbulent flows. Cambridge University Press

Preisser JS, Chestnutt D (1984) Flight effects on fan noise with static and wind-tunnel comparisons. J Aircr 217:453–461. https://doi.org/10.2514/3.44993

Tapken U, Caldas L, Meyer R, et al (2021a) New test facility to investigate the noise generated by shrouded fans for small aircraft applications. In: DICUAM, 15-17 March, Delft, The Netherlands

Tapken U, Caldas L, Meyer R, et al (2021b) Fan test rig for detailed investigation of noise generation mechanisms due to inflow disturbances. In: AIAA AVIATION 2021 Forum, VIRTUAL EVENT, pp 2-6. https://doi.org/10.2514/6.2021-2314